Performance of a Kinetic Inductance Traveling-Wave Parametric Amplifier at 4 Kelvin: Toward an Alternative to Semiconductor Amplifiers

M. Malnou, J. Aumentado, M.R. Vissers, J.D. Wheeler, J. Hubmayr, J.N. Ullom, and J. Gao

Performance of a Kinetic-Inductance Traveling-Wave Parametric Amplifier at 4 Kelvin: Toward an Alternative to Semiconductor Amplifiers

M. Malnou,[1, 2, *] J. Aumentado,[1] M. R. Vissers,[1] J. D. Wheeler,[1] J. Hubmayr,[1] J. N. Ullom,[1, 2] and J. Gao[1, 2]

[1]*National Institute of Standards and Technology, Boulder, Colorado 80305, USA*
[2]*Department of Physics, University of Colorado, Boulder, Colorado 80309, USA*
(Dated: March 22, 2022)

Most microwave readout architectures in quantum computing or sensing rely on a semiconductor amplifier at 4 K, typically a high-electron mobility transistor (HEMT). Despite its remarkable noise performance, a conventional HEMT dissipates several milliwatts of power, posing a practical challenge to scale up the number of qubits or sensors addressed in these architectures. As an alternative, we present an amplification chain consisting of a kinetic-inductance traveling-wave parametric amplifier (KI-TWPA) placed at 4 K, followed by a HEMT placed at 70 K, and demonstrate a chain-added noise $T_\Sigma = 6.3 \pm 0.5$ K between 3.5 and 5.5 GHz. While, in principle, any parametric amplifier can be quantum limited even at 4 K, in practice we find the KI-TWPA's performance limited by the temperature of its inputs, and by an excess of noise $T_{\rm ex} = 1.9$ K. The dissipation of the KI-TWPA's rf pump constitutes the main power load at 4 K and is about one percent that of a HEMT. These combined noise and power dissipation values pave the way for the KI-TWPA's use as a replacement for semiconductor amplifiers.

I. INTRODUCTION

Superconducting parametric amplifiers have been studied and refined for decades [1–8], yet they have always been used in the same configuration: as pre-amplifiers placed at millikelvin temperatures, followed by a 4 K stage low noise amplifier, conventionally a high-electron mobility transistor (HEMT). While Al-based parametric amplifiers can only operate well below the critical temperature of aluminum ($T_c \sim 1.2$ K), Nb-based Josephson amplifiers ($T_c \sim 9$ K) [2, 5, 9], or NbTiN-based kinetic amplifiers ($T_c \sim 14$ K) [4, 8, 10–12] can operate at much higher temperatures, in particular at 4 K.

At 4 K, HEMTs are commercially available and typically achieve input noise temperatures of a just few kevlins, with bandwidths spanning several gigahertz. They are integral to superconducting quantum computer architectures [13], to dark matter searches [14–16], and to the readout of superconducting transition-edge sensors or microwave kinetic inductance detectors [17, 18]. However, cryogenic HEMTs require several milliwatts of power, and the dissipated heat load can quickly become a serious challenge when designing experiments that require scaling to massive detector or qubit channel counts. For example, in both the Lynx [19, 20] and Origin Space Telescope [21–23], two of the four large mission concepts for observatories presented in the 2020 Astronomy and Astrophysics Decadal Survey [24], about 10 HEMTs are planned to measure signals from roughly 10,000 readout channels, and the power dissipation from the HEMTs is the single largest power load on the 4 K stage of the instrument. In space, achieving 10 mW of cooling power at 4 K is extremely challenging, therefore techniques for measuring gigahertz signals that can reduce this heat load are of great interest.

At millikelvin temperatures, the NbTiN-based kinetic-inductance traveling-wave parametric amplifier (KI-TWPA) has shown promising performance [4, 8, 10, 11, 25, 26]. In particular, its gigahertz bandwidth along with nanowatt input saturation power makes it compatible with high channel count applications, and it can operate close to the quantum limit [8, 25]. Furthermore, NbTiN resonators have internal quality factors $Q \gtrsim 10^3$ at 4 K due to their high T_c [27], so the KI-TWPA chip should be almost dissipation-less. In addition, the three-wave mixing (3WM) mode of operation has reduced its pump power requirements to the few microwatts range [8, 28], suggesting that the power dissipation at 4 K can be made much smaller than that generated by common HEMTs.

In this article, we ask– can a KI-TWPA replace a conventional 4 K stage semiconductor amplifier? Although one might expect parametric gain at 4 K, can one also expect it to retain its noise performance at such high temperature? Here we show that, in principle, a "hot" parametric amplifier can be quantum-limited, as long as its input fields are well-thermalized to a cold bath. Using a shot-noise tunnel junction (SNTJ), we measure the total chain-added noise of an amplification chain configured with the KI-TWPA at 4 K, followed by a HEMT placed at 70 K, and find $T_\Sigma = 6.3 \pm 0.5$ K between 3.5 and 5.5 GHz. This noise level is comparable to that of a well-optimized chain with a single HEMT placed at 4 K. Accounting for the contribution of each stage in the amplification chain, we estimate that the KI-TWPA alone generates 1.9 ± 0.2 K of excess noise, on par with the noise added by most commercial HEMTs [29]. Meanwhile, the power load at 4 K, predominantly due to dissipating the rf pump, is currently about 100 µW, or one percent that of a HEMT. Together, these measurements pave the way toward a more power efficient and lower noise alternative to semiconductor amplifiers at 4 K.

II. THEORY AND EXPERIMENTAL PRINCIPLE

The fundamental limit on the noise added by a lossless, phase-insensitive parametric amplifier is often described as originating from an internal mode [30–32]. But this mode is not an inaccessible internal degree of freedom. Rather, it refers to the input "idler" mode, and therefore this ideal amplifier should properly be described as a 4-port device: two inputs and two outputs, at the signal and idler frequencies (the idler output is usually not monitored). In this context, the mean amplifier output signal power is, in units of photons [8]:

$$N_{\text{out}}^s = G N_{\text{in}}^s + (G - 1) N_{\text{in}}^i, \tag{1}$$

where G is the amplifier signal power gain and N_{in}^s (N_{in}^i) is the input power at the signal (idler) frequency. Here, regardless of its physical temperature, the quantum-limited nature of the amplifier only depends on the input idler state: when it is vacuum $N_{\text{in}}^i = 1/2$, in the high gain limit the amplifier adds half a photon worth of noise energy to the input-referred signal N_{in}^s.

To test whether a "hot" parametric amplifier can remain quantum-limited, we design the amplification chain illustrated in Fig. 1, where a KI-TWPA is placed at 4 K, but whose signal and idler inputs are connected to the millikelvin stage. Then, provided that (i) the KI-TWPA's gain is enough overcome the following loss and amplifier-added noise, (ii) the KI-TWPA's inputs are cold, and (iii) the KI-TWPA is lossless, i.e. does not add any excess of noise on top of that from its inputs, the noise added by the entire chain should reach the quantum limit (half a photon), see appendix A 1.
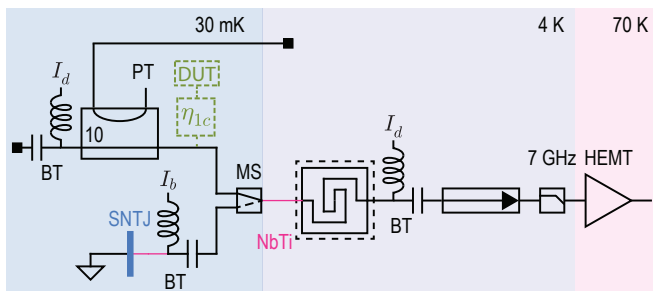

FIG. 1. Schematic of the amplification chain. The KI-TWPA (squared spiral) is magnetically shielded (dashed square) and placed at 4 K while the HEMT operates at 70 K, protected from the strong KI-TWPA pump tone (PT) by a low pass filter. The PT then dissipates into the isolator (4-12 GHz). When the microwave switch (MS) is in its top position, the PT is delivered to the KI-TWPA via a directional coupler (DC), while two bias tees (BT) allow the dc current I_d to flow in and out of the chain, through the KI-TWPA. A hypothetical DUT is coupled to the chain with efficiency η_{1c}. When the MS is in its bottom position, the SNTJ delivers a known noise [33] to the chain's input, whose power depends on the current I_b (delivered via a BT) with which the SNTJ is biased.

Operating the KI-TWPA in a 3WM fashion [8, 26], we employ a bias tee (BT) and a directional coupler (DC) to deliver respectively a dc current and an rf pump to its physical input port. Both BT and DC are placed at 30 mK, behind a hypothetical device under test (DUT) coupled to the readout line thereby minimizing insertion loss between DUT and KI-TWPA. This configuration is particularly suitable when the DUT represents an array of resonators, such as microwave kinetic-inductance detectors [25, 34], or a microwave superconducting quantum interference device multiplexer [35, 36].

To measure the added noise of such a chain, we insert a microwave switch (MS) that allows us to alternate between the KI-TWPA biasing components and a calibrated noise source, consisting of a shot noise tunnel junction (SNTJ) [8, 37]. We first obtain the added noise N_{Σ}' of the chain when the MS is toggled toward the SNTJ (see appendix E 1). Then, after actuating the MS, we turn on the KI-TWPA and measure the level r to which the output noise rises. We then deduce the chain-added noise N_{Σ} using

$$\frac{r}{G} = \frac{N_{\Sigma} + N_c}{N_{\Sigma}' + N_c}, \tag{2}$$

where G is the KI-TWPA gain and N_c the vacuum noise, see appendix A 2.

III. PERFORMANCE AT 4 K

The results of such a measurement are presented in Fig. 2, performed when using a commercial HEMT and a KI-TWPA, whose design and millikelvin performance have been described elsewhere [8]. With the MS actuated toward the DC and BT, we operate the KI-TWPA at various gains, from an average of 2.5 dB, to 18 dB between 3.5 and 5.5 GHz, see Fig. 2(a); the higher gain profile remains flat, with less than 3 dB ripples in that band. For each operating gain G, we record the noise rise r on a spectrum analyzer (SA) and form $T_{\Sigma} = N_{\Sigma} \hbar \omega / k_B$ (with $\hbar$ the reduced Planck constant and k_B the Boltzmann constant) using Eq. 2. In Fig. 2(b), we show T_{Σ} as a function of frequency, when the KI-TWPA is operated at low and high gain (gray and black curves, respectively), along with $T_{\Sigma}' = N_{\Sigma}' \hbar \omega / k_B$, obtained when the MS is actuated toward the SNTJ (purple curve). At high gain, $T_{\Sigma} = 6.3 \pm 0.5$ K between 3.5 and 5.5 GHz (with uncertainty dominated by that of the chain's output power, known within ± 0.3 dB). To our knowledge, it is the first time that such a low and broadband noise performance has been obtained without the use of a semiconductor amplifier at 4 K.

As discussed in Sec. II, three possible sources of noise prevent T_{Σ} to reach the quantum limit: (i) insufficient KI-TWPA gain, (ii) warm KI-TWPA inputs, and (iii) KI-TWPA-excess noise. Although from a user perspective only T_{Σ} matters, knowing the separate contribution of these sources is interesting from an amplifier-design perspective, because it indicates if and how T_{Σ} may be
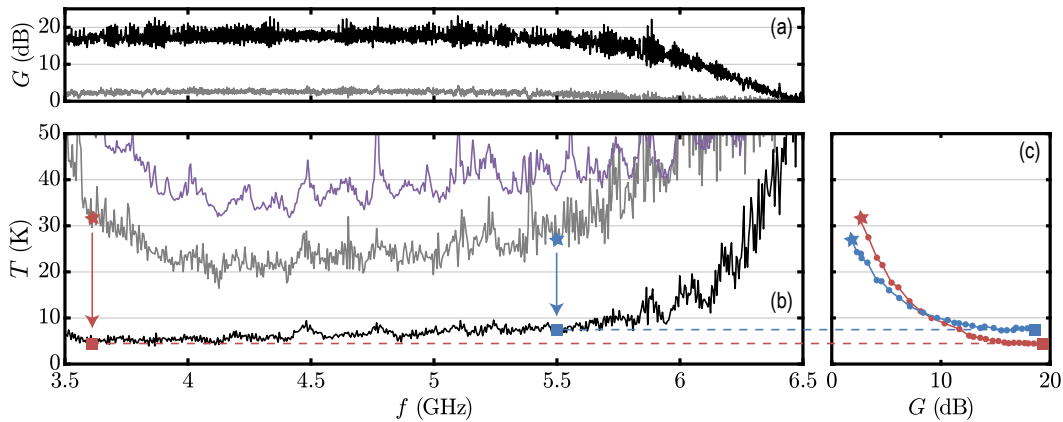
FIG. 2. Chain-added noise measurement. (a) The KI-TWPA gain G (ratio pump on/off) as a function of frequency (measured with a vector network analyzer) is shown for two rf pump powers (P_p): at low pump power (gray curve, $P_p = -37\,\text{dBm}$ at the KI-TWPA's input) and high pump power (black curve, $P_p = -29\,\text{dBm}$). In both cases, the pump frequency is $f_p = 8.979\,\text{GHz}$, and the KI-TWPA is dc biased with $I_d = 0.7\,\text{mA}$. (b) We first measured the frequency-dependent chain-added noise T'_Σ (purple curve) with the SNTJ. Below 4 GHz and above 6 GHz, T'_Σ increases because we reach the pass-band edge of the components in the amplification chain (HEMT, isolator and low-pass filter). Then, we deduced the chain-added noise T_Σ when the KI-TWPA operates at the low (gray curve) and high (black curve) gain G presented in panel (a). Points at two witness frequencies (3.6 GHz and 5.5 GHz) underline how the noise diminishes (from stars to squares) when the gain increases. (c) At these two frequencies, the variation of T_Σ as a function of gain shows that the lowest noise temperature (square) reaches an asymptote.

improved. In Fig. 2(c) we present the variation of T_Σ as a function of G, at two different frequencies. As G increases, T_Σ reaches an asymptotic lower bound. Therefore, the high gain regime of our KI-TWPA is enough to overcome the following loss and HEMT-added noise; operating at higher gain would not improve the chain-added noise.

To evaluate the noise coming from the KI-TWPA inputs, we separately measure at 4 K the transmission efficiencies of each stage in the amplification chain, see appendix F. Each efficiency acts as an effective noise source, whose temperature is governed by a beamsplitter interaction (see appendix A 1). In Tab. I we report the transmission efficiencies and corresponding noise temperatures of the various stages, either when considered separately (intrinsic noise) or within the amplification chain (chain-input-referred noise). Clearly, the temperature of the KI-TWPA inputs is dominated by the effect of $\eta_{1h} = 0.8$, the transmission efficiency at 4 K between the DUT and the KI-TWPA. It generates 2.1 K of noise at the input of the amplifier (and 2.6 K when referred to the input of the chain). Practically, T_Σ may be significantly decreased with increasing η_{1h}: for example with $\eta_{1h} = 0.9$, T_Σ would drop from 6.3 K to 4.5 K. We believe this performance achievable, because most of our warm insertion loss originates in the KI-TWPA packaging, whose printed-circuit boards and connectors may be made less dissipative.

Subtracting the (input-referred) noise generated by all the inefficient transmissions from T_Σ, we deduce the KI-TWPA-excess noise: at the chain's input, it amounts to 2.9 K, equivalent to an intrinsic excess noise temperature $T_{\text{ex}} = 1.9 \pm 0.2\,\text{K}$, on par with that of the HEMT at 4 K

[29]. This noise is associated to some internal loss, see appendix B.

sources of noise	η_{1c}	η_{1h}	G	η_2	G_H
transmission efficiency	0.80	0.80	–	0.51	–
insertion loss (dB)	1	1	–	2.9	–
intrinsic noise (K)	0.16	2.1	1.9	3.9	10.7
input-referred noise (K)	0.16	2.6	2.9	0.1	0.6

TABLE I. Noise contribution of each stage of the amplification chain, averaged between 3.5 and 5.5 GHz. DUT signals are routed to the amplifier's signal input with efficiency η_{1c} at 30 mK (i.e. there is $-10\log(\eta_{1c})$ dB of insertion loss) and with efficiency η_{1h} at 4 K. After the KI-TWPA, signals are routed with efficiency η_2 to the HEMT input, see appendix A 1. From the transmission efficiencies, we calculate the intrinsic and chain-input-referred noise temperatures, using the expressions reported in Tab. III. Note that for the noises related to η_{1c} and η_{1h}, the contribution of the signal and idler paths have been added. The intrinsic HEMT-added noise at 70 K (first stage of our dilution refrigerator) $T_H = 13.4 \pm 0.4\,\text{K}$ lies between the HEMT-added noise at 4 K and that at 296 K [29].

As a fair comparison to T_Σ, we measured the noise temperature $T_{\Sigma 2}$ added by a well-optimized chain, employing only a HEMT at 4 K (see appendix D). Between 3.5 and 5.5 GHz, $T_{\Sigma 2} = 3.5 \pm 0.3\,\text{K}$ (with uncertainty here

dominated by that of the SNTJ impedance, $48.2 \pm 3.5 \, \Omega$). Therefore, while not surpassing it, the KI-TWPA-based solution approaches the HEMT-based performance.

IV. POWER CONSUMPTION

In combination with having a competitive amplification and noise performance compared to that of a HEMT, the 4 K stage KI-TWPA is expected to consume much less power. In fact, it typically requires an rf pump power $P_p \sim -30 \, \mathrm{dBm}$ (i.e. 1 μW), several orders of magnitude lower than the power requirement for a standard ($\sim 10 \, \mathrm{mW}$ [29]) or even state-of-the-art ($300 \, \mu\mathrm{W}$ [38]) HEMT. Note however that P_p does not account for the dissipation along the pump line. In our current setup, the pump travels to the KI-TWPA via a 10 dB attenuator at 4 K, and through the weakly coupled port of a 10 dB DC at the millikelvin stage, see appendix C 1. Therefore in our experiment, a typical $-30 \, \mathrm{dBm}$ pump tone delivered to the KI-TWPA translates into dissipating 99 μW at 4 K (the DC being terminated at 4 K). But such a heavy attenuation is not mandatory: in principle, the high-pass filter (HPF) we employ at the millikelvin stage suffices to prevent the room temperature 300 K noise to directly contaminate the signal and idler bands. At the pump frequency, this noise is negligible compared to the tone's power and therefore does not affect the dynamics of the KI-TWPA (in the limit of non-diverging gain [12]). So instead of being injected through the 4 K stage attenuator and millikelvin stage DC, the pump could simply pass through the HPF and enter the rf port of the input bias tee. Furthermore, at 4 K, P_p is currently dissipated in the isolator placed before the HEMT, which could also be avoided by using a diplexer to redirect the pump to higher temperature. With these strategies, the dissipation associated with the pump can be reduced below 1 μW at 4 K. Further possible improvements of the amplification chain, in particular targeted for qubit readout applications, are discussed in appendix C 2.

But the KI-TWPA also requires a non-negligible dc bias $I_d \sim 1 \, \mathrm{mA}$, which may dissipate and generate heat. We measured the corresponding dissipated power P_d with a four-point probe setup (see appendix G): reading the voltage drop V_d across the KI-TWPA, we then retrieve $P_d = V_d I_d$. In Fig. 3 we show P_d as function of I_d, when the rf pump is off (solid black line) or instead, very strong ($P_p = -20 \, \mathrm{dBm}$, dashed black line). In both cases, at $I_d = 1 \, \mathrm{mA}$ we obtain $P_d \simeq 100 \, \mathrm{nW}$, several orders of magnitude lower than what a HEMT consumes. We also show the resistance $R_d = V_d / I_d$ (right y-axis) as a function of I_d. Under normal operation, i.e. for $I_d < 1.5 \, \mathrm{mA}$, the resistance across the four-point probes (encompassing the KI-TWPA, its packaging, and the BT at 4 K) is $R_d = 80 \, \mathrm{m\Omega}$. Conversely, R_d sharply increases to $\sim 1 \, \mathrm{k\Omega}$ when $I_d > 1.5 \, \mathrm{mA}$, because superconductivity breaks down inside the KI-TWPA, probably at a weak link [8, 39]. Note that the transition to this dissipative regime

happens at slightly reduced I_d when $P_p = -20 \, \mathrm{dBm}$, suggesting that both the dc and rf currents can activate the weak link. Voltage biasing the KI-TWPA with a small ($\sim 100 \, \Omega$) shunting resistor would alleviate transitioning to this regime.
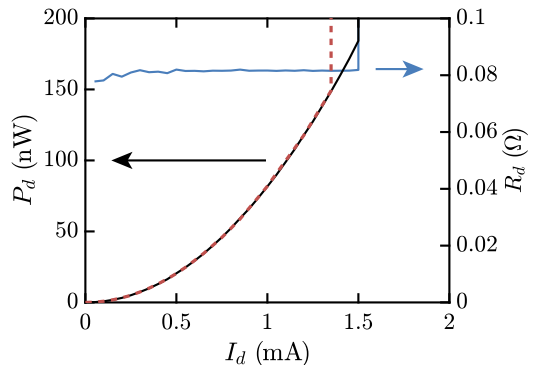

FIG. 3. Characterization of the KI-TWPA dc power dissipation. The dissipated power P_d (left y-axis) is shown as a function of the bias current I_d for two situations: when the KI-TWPA's pump is off (solid black line) and when $P_p = -20 \, \mathrm{dBm}$ (dashed red line). In the pump-off situation, the resistance R_d (right y-axis) is also shown as a function of I_d (blue curve).

V. CONCLUSION

Despite their remarkable noise performance at 4 K, semiconductor amplifiers remain power hungry. This dissipation may limit the scale of future applications, for which large arrays ($> 10^5$) of detectors or qubits would require tens to hundreds of low noise amplifiers. As an alternative, we investigated the use of a parametric amplifier at 4 K: the KI-TWPA. Using a SNTJ as a calibrated noise source, we measured the noise added by an amplification chain where the KI-TWPA is the sole 4 K stage amplifier. In principle, this chain can remain quantum limited; in practice, when the KI-TWPA is operated at an average gain of 18 dB within a 2 GHz bandwidth (and with less than 3 dB gain ripples in that band) we measured an average chain-added noise of $6.3 \pm 0.5 \, \mathrm{K}$, comparable to that of a chain where the HEMT is the 4 K stage amplifier. This performance is limited mostly by the insertion loss at 4 K preceding the KI-TWPA, and by an excess of noise $T_{\mathrm{ex}} = 1.9 \pm 0.2 \, \mathrm{K}$. Furthermore, the heat load at 4 K, currently in the 100 μW range, is due to dissipating the rf pump. It is two orders of magnitude lower than what a conventional HEMT generates, and can straightforwardly be reduced below 1 μW. To our knowledge this work is the first successful implementation of a broadband, high-gain, low noise, and power-efficient microwave parametric amplifier at 4 K. As such, our work constitutes a shift in the readout architecture for large numbers of microwave resonators.

Appendix A: Added noise

1. Chain-added noise

Figures 4(a) and 4(b) recast the amplification chain presented in Fig. 1 in a diagram of cascaded transmission efficiencies and gains, when the microwave switch (MS) is activated toward the KI-TWPA biasing components [Fig. 4(a)], or toward the SNTJ [Fig. 4(b)]. Considering the situation in Fig. 4(a) first, a signal with photon number N_{in}^s at the chain's input (that would be generated by the hypothetical DUT), undergoes amplification and loss when propagating to the chain:

$$N_{1c}^s = \eta_{1c}\left(N_{\mathrm{in}}^s + \frac{1-\eta_{1c}}{\eta_{1c}}N_c\right) \tag{A1}$$

$$N_{1h}^s = \eta_{1h}\left(N_{1c}^s + \frac{1-\eta_{1h}}{\eta_{1h}}N_h\right) \tag{A2}$$

$$N_{1h}^i = \eta_{1h}^i\left(N_c + \frac{1-\eta_{1h}^i}{\eta_{1h}^i}N_h\right) \tag{A3}$$

$$N_2^s = G(N_{1h}^s + N_{\mathrm{ex}}^s) + (G-1)(N_{1h}^i + N_{\mathrm{ex}}^i) \tag{A4}$$

$$N_3^s = \eta_2\left(N_2^s + \frac{1-\eta_2}{\eta_2}N_h\right) \tag{A5}$$

$$N_4^s = G_H(N_3^s + N_H), \tag{A6}$$

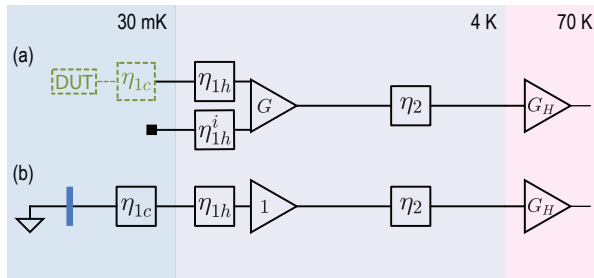where the variables are all defined in Tab II.

FIG. 4. Diagram of cascaded transmission efficiencies and gains, when the MS is activated toward the KI-TWPA biasing components (a), or toward the SNTJ (b).

Variable name	Definition
N_{in}^s	chain's input signal
N_c	Vacuum noise
N_{1c}^s	Cold stage output signal
N_h	4 K stage thermal noise
N_{1h}^s	KI-TWPA input signal
N_{1h}^i	KI-TWPA input idler
N_{ex}^s	Signal-to-signal path KI-TWPA-excess noise
N_{ex}^i	Idler-to-signal path KI-TWPA-excess noise
N_{ex}	overall KI-TWPA-excess noise
N_H	HEMT-added noise
N_2^s	KI-TWPA output signal
N_3^s	HEMT input signal
N_4^s	HEMT output signal
η_{1c}	cold stage signal transmission efficiency
η_{1h}	4 K stage signal transmission efficiency
η_{1h}^i	4 K stage idler transmission efficiency
η_2	KI-TWPA to HEMT transmission efficiency
G	KI-TWPA signal power gain
G_H	HEMT signal power gain

TABLE II. List of the variables pertaining to the amplification chain, Figs. 1b and c. The variables designating a power (named with N) are in units of quanta. The transmission efficiencies are dimensionless, and the gains are linear.

Assuming that the HEMT gain is sufficient to overcome any following loss and amplifier-added noise, the power at the signal frequency reaching the spectrum analyzer (SA) is directly proportional to N_4^s. Using Eqs. A1 to A6, and in the simpler case where $G \gg 1$ and where idler and signal transmission efficiencies at 4 K are equal, $\eta_{1h}^i = \eta_{1h}$, we have

$$N_4^s = G_H \eta_2 G \eta_{1h} \eta_{1c}(N_{\mathrm{in}}^s + N_\Sigma), \tag{A7}$$

where

$$\begin{aligned}
N_\Sigma =& \frac{2-\eta_{1c}}{\eta_{1c}}N_c + 2\frac{1-\eta_{1h}}{\eta_{1h}\eta_{1c}}N_h + \frac{1}{\eta_{1h}\eta_{1c}}N_{\mathrm{ex}} \\
&+ \frac{1-\eta_2}{\eta_2 G \eta_{1h}\eta_{1c}}N_h + \frac{1}{\eta_2 G \eta_{1h}\eta_{1c}}N_H,
\end{aligned} \tag{A8}$$

is the chain-added noise. The first line on the right-hand side of Eq. A8 can be identified to the KI-TWPA-added noise; it depends not only on the KI-TWPA-excess noise $N_{\mathrm{ex}} = N_{\mathrm{ex}}^s + N_{\mathrm{ex}}^i$, but also on the cold and warm transmission efficiencies between the KI-TWPA and the chain's input. The second line represents the contributions of the elements placed after the KI-TWPA: transmission efficiency η_2 (first term) and HEMT-added noise (second term); they are damped at sufficiently high gain G. In the high gain limit, with perfect transmission efficiencies $\eta_{1c} = \eta_{1h} = 1$ (i.e. the KI-TWPA's inputs are perfectly thermalized to the cold bath) and without excess noise

($N_{\rm ex} = 0$), we verify that $N_\Sigma = 1/2$, the minimum chain-added noise.

All the terms in Eq. A8 are referred to the chain's input: the noise from each source is divided by the transmission efficiencies and gain preceding it. Conversely, the noise intrinsic to each stage is chain-independent. The expressions for the chain-input-referred and intrinsic noise for each stage is reported in Tab III.
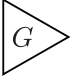
sources of noise	chain-input-referred noise	intrinsic noise
$\boxed{\eta_{1c}}$	$\frac{2-\eta_{1c}}{\eta_{1c}}N_c$	$\frac{2-\eta_{1c}}{\eta_{1c}}N_c$
$\boxed{\eta_{1h}}$	$2\,\frac{1-\eta_{1h}}{\eta_{1h}\eta_{1c}}N_h$	$2\frac{1-\eta_{1h}}{\eta_{1h}}N_h$
$\triangleright G$	$\frac{1}{\eta_{1h}\eta_{1c}}N_{\rm ex}$	$N_{\rm ex}$
$\boxed{\eta_2}$	$\frac{1-\eta_2}{\eta_2 G\eta_{1h}\eta_{1c}}N_h$	$\frac{1-\eta_2}{\eta_2}N_h$
$\triangleright G_H$	$\frac{1}{\eta_2 G\eta_{1h}\eta_{1c}}N_H$	N_H

TABLE III. Noise generated by each stage in the amplification chain.

To calculate N'_Σ (the chain-added noise when the KI-TWPA is off and the MS actuated toward the SNTJ), we propagate the SNTJ calibrated noise $N^s_{\rm in}$ (which is our 'signal') through the chain shown in Fig. 4(b). Here, η_{1c} accounts for the cold loss coming in particular from the SNTJ packaging and from the following BT. Meanwhile, the unpumped KI-TWPA acts as a passive element of gain 1, therefore we need not keep track of the noise entering the idler port [8, 40], because the KI-TWPA output signal does not contain the idler component, as can be seen from Eq. 1. We thus obtain the HEMT-output signal power

$$N_4^{s'} = G_H \eta_2 \eta_{1h} \eta_{1c}(N^s_{\rm in} + N'_\Sigma), \tag{A9}$$

with

$$\begin{aligned} N'_\Sigma &= \frac{1-\eta_{1c}}{\eta_{1c}}N_c + \frac{1-\eta_{1h}}{\eta_{1h}\eta_{1c}}N_h \\ &+ \frac{1-\eta_2}{\eta_2\eta_{1h}\eta_{1c}}N_h + \frac{1}{\eta_2\eta_{1h}\eta_{1c}}N_H. \end{aligned} \tag{A10}$$

Varying $N^s_{\rm in}$, we retrieve N'_Σ. Then, knowing the transmission efficiencies from the loss budget (see appendix F), we can calculate N_H.

2. Noise rise

The noise rise measurement consists of comparing the output noise power, recorded on the SA, when the KI-TWPA is on and off; knowing G and N'_Σ, we can retrieve N_Σ.

With the MS actuated toward the KI-TWPA, the HEMT-output noise obtained with the KI-TWPA off (pump off, no dc bias) is equal to that of Eq. A9 (assuming the loss between the two MS paths equal, and that signals from the DUT would be transmitted with efficiency η_{1c} at 30 mK). But here, $N^s_{\rm in} = N_c$, because there is vacuum noise at the chain's signal input. Similarly, the HEMT-output noise obtained with the KI-TWPA on is equal to that of Eq. A7, with $N^s_{\rm in} = N_c$, such that the ratio of output noises r is

$$r = G\frac{N_\Sigma + N_c}{N'_\Sigma + N_c}, \tag{A11}$$

which gives Eq. 2.

Appendix B: Excess of noise and internal loss

The excess of noise in the KI-TWPA is associated with internal loss. Here we evaluate this loss, and show that it generates a noise commensurate with our observed excess noise of 1.9 K. We then discuss the possible origins of this loss.

1. From internal loss to transmission efficiency

Material loss can be characterized by the internal quality factor Q_i that a resonator fabricated in that material would have, or equivalently by its loss tangent $\tan\delta = 1/Qi$. In our case, we measured $Q_i \simeq 5000$ on an NbTiN resonator at 4 K whose characteristics (line width, dc bias) are similar to that of the KI-TWPA.

In turn, Q_i can be expressed as a function of the field propagation constant $\alpha + i\beta$ in that material, as $Q_i = \beta/(2\alpha)$. Here, $\beta = k = \omega/v_p$ (excluding any dispersion engineering) with v_p the phase velocity, and α is the (amplitude) attenuation constant. In our KI-TWPA, $v_p = \lambda_s f_s \simeq 1000$ cells/ns, where λ_s is the wavelength of the periodic loading pattern that creates a stop-band at frequency f_s [8]. Thus, with $Q_i = 5000$ and at $\omega = 2\pi \times 4.5$ GHz, we obtain $\alpha \simeq 2.8 \times 10^{-6}$ cell^{-1}.

Our KI-TWPA contains $C_t = 66000$ cells, therefore the total transmission efficiency is $\eta_0 = \exp(-2\alpha C_t) \simeq 0.69$. In other words, the total insertion loss in the KI-TWPA is equal to 1.6 dB. If we were to place this entire loss at the KI-TWPA signal and idler inputs, it would generate an excess noise $T_{\rm ex} = 3.6$ K for an effective gain $G = 18$ dB. However, this loss is distributed along the line, and that is why this naive calculation clearly over-estimates the noise generated by this loss.

2. Excess noise from a distributed loss

The effect of distributed (and potentially asymmetric) loss on the ideal exponential gain of a traveling-wave parametric amplifier has been treated in theory [30, 41]. Here, we distribute a known effective power gain G (that need not be perfectly exponential) and total transmission efficiency η_0 within several stages, to evaluate the excess of noise associated with this distribution.

When the phase matching condition is achieved in a traveling-wave parametric amplifier of length x, the output currents $\tilde{A}(x)$ and $\tilde{B}^*(x)$ at the signal and idler frequencies are [8, 42]

$$\begin{aligned} \tilde{A}(x) &= A(x)e^{i2\chi k_a x} \\ \tilde{B}^*(x) &= B^*(x)e^{i2\chi k_b x}, \end{aligned} \tag{B1}$$

where χ is the cross-phase modulation term, and k_a (k_b) is the wavenumber at the signal (idler) frequency. The amplitudes $A(x)$ and $B^*(x)$ are given by

$$\begin{pmatrix} A(x)/\sqrt{k_a} \\ B^*(x)/\sqrt{k_b} \end{pmatrix} = \\ \begin{pmatrix} \cosh{(g_3 x)} & i\sinh{(g_3 x)} \\ -i\sinh{(g_3 x)} & \cosh{(g_3 x)} \end{pmatrix} \begin{pmatrix} A(0)/\sqrt{k_a} \\ B^*(0)/\sqrt{k_b} \end{pmatrix}. \tag{B2}$$

In other words, for a given length of line x, the amplitude (i.e. gain) and phase of the currents are separately determined.

We now describe the signal and idler modes in terms of number operators. Their phase is determined by Eq. B1. Then, for an amplifier with signal power gain G_0, preceded by a transmission transmission efficiency η_0 (modeled as a beamsplitter interaction) the input modes' amplitudes a_{in} and b_{in} are transformed into the output modes' amplitudes a_{out} and b_{out} according to

$$\begin{pmatrix} a_{\mathrm{out}} \\ b_{\mathrm{out}}^\dagger \end{pmatrix} = \begin{pmatrix} \sqrt{\eta_0 G_0} & i\sqrt{\eta_0(G_0-1)} \\ -i\sqrt{\eta_0(G_0-1)} & \sqrt{\eta_0 G_0} \end{pmatrix} \begin{pmatrix} a_{\mathrm{in}} \\ b_{\mathrm{in}}^\dagger \end{pmatrix}. \tag{B3}$$

The effective signal gain power G (as observed on the VNA) is therefore equal to $\eta_0 G_0$. Considering now that the line has been divided into n identical stages (see Fig. 5) each characterized by a transmission efficiency η_n and gain G_n, the amplitude of the output modes is given by:

$$\begin{aligned} \begin{pmatrix} a_{\mathrm{out}} \\ b_{\mathrm{out}}^\dagger \end{pmatrix} &= \begin{pmatrix} \sqrt{\eta_n G_n} & i\sqrt{\eta_n(G_n-1)} \\ -i\sqrt{\eta_n(G_n-1)} & \sqrt{\eta_n G_n} \end{pmatrix}^n \begin{pmatrix} a_{\mathrm{in}} \\ b_{\mathrm{in}}^\dagger \end{pmatrix} \\ &= \begin{pmatrix} g_{\mathrm{aa}}(n) & g_{\mathrm{ab}}(n) \\ g_{\mathrm{ba}}(n) & g_{\mathrm{bb}}(n) \end{pmatrix} \begin{pmatrix} a_{\mathrm{in}} \\ b_{\mathrm{in}}^\dagger \end{pmatrix}, \end{aligned} \tag{B4}$$

where

$$g_{\mathrm{aa}}(n) = \frac{1}{2}\Bigg[\left(\sqrt{\eta_n G_n} + \sqrt{\eta_n(G_n-1)}\right)^n \\ + \left(\sqrt{\eta_n G_n} - \sqrt{\eta_n(G_n-1)}\right)^n \Bigg] \tag{B5}$$

and

$$g_{\mathrm{ab}}(n) = -i\frac{1}{2}\Bigg[\left(\sqrt{\eta_n G_n} + \sqrt{\eta_n(G_n-1)}\right)^n \\ - \left(\sqrt{\eta_n G_n} - \sqrt{\eta_n(G_n-1)}\right)^n \Bigg], \tag{B6}$$

and with $g_{\mathrm{aa}}(n) = g_{\mathrm{bb}}(n)$ and $g_{\mathrm{ab}}(n) = -g_{\mathrm{ba}}(n)$. These relations define, for any number of stages n, the relation between $\{\eta_n, G_n\}$ and $\{\eta_0, G_0\}$, because for any n, the overall signal and idler amplitude gain is always equal to $\sqrt{\eta_0 G_0}$ and $i\sqrt{\eta_0(G_0-1)}$, respectively. But we can more easily calculate η_n and G_n in a recursive manner when $n = 2^p$ where $p \in \mathbb{N}$, because then

$$\eta_{2^p} = \sqrt{\eta_{2^{p-1}}} \tag{B7}$$

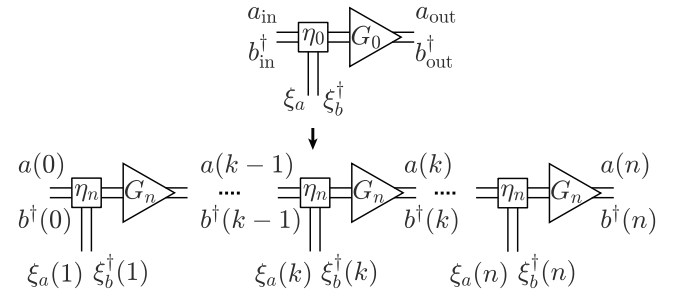$$G_{2^p} = \frac{\sqrt{G_{2^{p-1}}}+1}{2}. \tag{B8}$$

FIG. 5. A model for distributed amplification and loss along the KI-TWPA. Starting with an amplifier with power gain G_0 and a power transmission efficiency η_0, we divide the gain and loss along the KI-TWPA in n identical stages, each with transmission efficiency η_n and gain G_n.

We now introduce the loss modes $\xi_a(k)$ and $\xi_b(k)$ for $k \in \{1, n\}$, see Fig. 5. These modes are complex, each with a random phase. The output of stage k is then given by:

$$a(k) = \sqrt{\eta_n G_n}\, a(k-1) + \sqrt{\eta_n (G_n - 1)}\, b^\dagger(k-1) + \sqrt{(1-\eta_n) G_n}\, \xi_a(k) + \sqrt{(1-\eta_n)(G_n-1)}\, \xi_b^\dagger(k) \tag{B9}$$

$$b^\dagger(k) = \sqrt{\eta_n(G_n-1)}\, a(k-1) + \sqrt{\eta_n G_n}\, b^\dagger(k-1) + \sqrt{(1-\eta_n)(G_n-1)}\, \xi_a(k) + \sqrt{(1-\eta_n) G_n}\, \xi_b^\dagger(k). \tag{B10}$$

Thus, we obtain recursively

$$\begin{aligned} a(n) =& g_{\mathrm{aa}}(n) a(0) + g_{\mathrm{ab}}(n) b^\dagger(0) \\ &+ \sum_{j=1}^{n} \left(c_a(j) \xi_a(j) + c_b(j) \xi_b^\dagger(j) \right), \end{aligned} \tag{B11}$$

where, for $j \in \{1, n\}$,

$$\begin{aligned} c_a(j) =& g_{\mathrm{aa}}(n-j)\sqrt{(1-\eta_n) G_n} \\ &+ g_{\mathrm{ab}}(n-j)\sqrt{(1-\eta_n)(G_n-1)} \end{aligned} \tag{B12}$$

and

$$\begin{aligned} c_b(j) =& g_{\mathrm{aa}}(n-j)\sqrt{(1-\eta_n)(G_n-1)} \\ &+ g_{\mathrm{ab}}(n-j)\sqrt{(1-\eta_n) G_n}. \end{aligned} \tag{B13}$$

We now need to calculate $\langle a^\dagger(n) a(n)\rangle$. Here, we assume that the loss modes are all uncorrelated, and that they are all in equilibrium with a bath at temperature T_h, i.e. $\langle \xi_i^\dagger(k) \xi_j(l)\rangle = \delta_{\mathrm{ij}} \delta_{\mathrm{kl}} \bar{n}_h$, where $\bar{n}_h$ is the average photon number in each mode. We also assume that $a(0)$ and $b(0)$ are neither correlated to each other, nor to any of the loss modes. With these conditions, we have

$$\begin{aligned} \langle a^\dagger(n) a(n)\rangle =& |g_{\mathrm{aa}}(n)|^2 \left(\langle a^\dagger(0) a(0)\rangle + \frac{1}{2} \right) + |g_{\mathrm{ab}}(n)|^2 \left(\langle b^\dagger(0) b(0)\rangle + \frac{1}{2} \right) \\ &+ \sum_{j=1}^{n} |c_a(j)|^2 \left(\langle \xi_a^\dagger(j) \xi_a(j)\rangle + \frac{1}{2} \right) + |c_b(j)|^2 \left(\langle \xi_b^\dagger(j) \xi_b(j)\rangle + \frac{1}{2} \right) \\ &+ \frac{1}{2} \left(|g_{\mathrm{ab}}(n)|^2 - |g_{\mathrm{aa}}(n)|^2 + \sum_{j=1}^{n} |c_b(j)|^2 - |c_a(j)|^2 \right). \end{aligned} \tag{B14}$$

Finally, the last term of Eq. B14 is equal to $-1/2$ because $g_{\mathrm{ab}}^2(n) - g_{\mathrm{aa}}^2(n) = -\eta_n^n$ and because $|c_b(j)|^2 - |c_a(j)| = (1-\eta_n)\eta_n^j$, for $j \in \{1, n\}$. We thus obtain

$$N_{\mathrm{out}}^s = g_{\mathrm{aa}}^2(n) N_{\mathrm{in}}^s + g_{\mathrm{ab}}^2(n) N_{\mathrm{in}}^i + N_{\mathrm{ex}}, \tag{B15}$$

where

$$N_{\mathrm{ex}} = N_{\mathrm{h}} \sum_{j=1}^{n} \left(|c_a(j)|^2 + |c_b(j)|^2 \right). \tag{B16}$$

Here, $N_{\mathrm{out}}^s = \langle a^\dagger(n) a(n)\rangle + 1/2$, $N_{\mathrm{in}}^s = \langle a^\dagger(0) a(0)\rangle + 1/2$, $N_{\mathrm{in}}^i = \langle b^\dagger(0) b(0)\rangle + 1/2$, and $N_h = \langle \xi_a^\dagger(j) \xi_a(j)\rangle + 1/2 = \langle \xi_b^\dagger(j) \xi_b(j)\rangle + 1/2$, for $j \in \{1, n\}$. Equation B15 is the equivalent of Eq. 1 when accounting for a distributed loss within the traveling-wave parametric amplifier.

In practice, the excess noise quickly converges to an asymptotic value, as we increase the number of divisions n, because gain and loss equilibrate. At $n = 1024$ it can be considered as asymptotic. Starting with $\eta_0 = 0.69$ and $G = 18\,\mathrm{dB}$, we thus estimate that $T_{\mathrm{ex}} = 0.5\,\mathrm{K}$. Therefore,

it shows that the excess noise implied by the non-zero loss along the line is clearly non negligible. The discrepancy between this theoretical value and the experimental one $(1.9\,\mathrm{K})$ may come from uncertainties in the line's true attenuation constant (i.e. Q_i), but also in the possible inhomogeneous distribution of the loss, which may be greater at the beginning of the line.

3. Possible origin for the internal loss

Several phenomena can give rise to internal loss, including an excess of quasi-particles, two-level systems in the dielectric, or itinerant vortices. A recent study on an NbTiN transmission line embedded in an amorphous silicon matrix [11] suggests that itinerant vortices arise when dc-biasing the line. Further study is required to identify and quantify the various possible sources of loss.
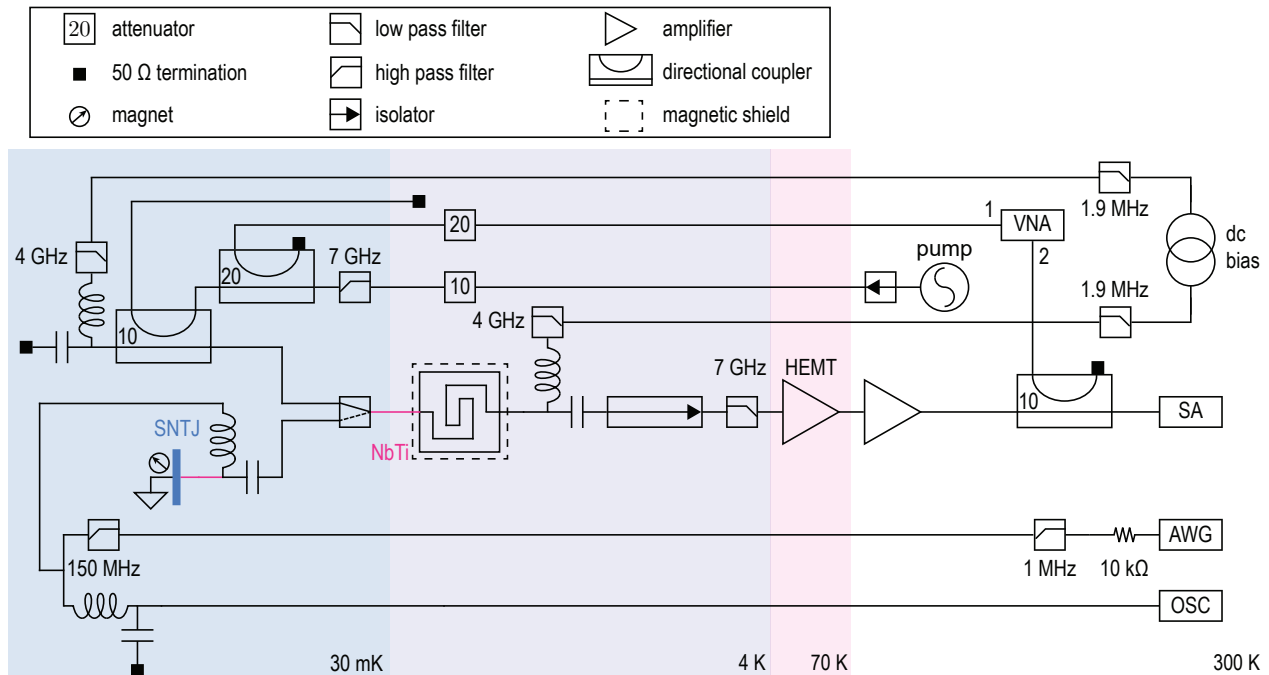
FIG. 6. Full experimental setup used to measure the KI-TWPA's noise performance at 4 K.

Appendix C: Full experimental setup

1. Existing setup

The full experimental setup used to measure the chain-added noise containing the KI-TWPA is shown in Fig. 6. It is composed of three main parts: the KI-TWPA control electronics (top), the amplification chain (middle) and the SNTJ control electronics (bottom). At the top, a current source and a microwave generator output respectively the dc and rf KI-TWPA biases. The high-pass filter on the pump line (ZHSS-8G-S+) provides over 30 dB of insetion loss at 6.5 GHz, and over 80 dB at 4 GHz. In addition, a vector network analyzer (VNA) is connected to the input and output of the amplification chain, allowing to measure the KI-TWPA gain.

In the middle, the amplification chain contains three amplifiers: the KI-TWPA at 4 K, the HEMT at 70 K, and a room temperature amplifier (LNA-30-00101200-17-10P). Signals from the millikelvin stage, either vacuum noise or calibrated noise from the SNTJ, depending on the microwave switch position, travel through these amplifiers and are read on the spectrum analyzer at room temperature.

Because of cable resistance between the SNTJ and its drive generator (the AWG), we cannot directly voltage bias the SNTJ. Instead, we current bias it with I_b (through a $10 \, \text{k}\Omega$ polarization resistor) and retrieve $V = R_{\text{SNTJ}} I_b$ by first measuring the SNTJ resistance R_{SNTJ}. To do that, we send a known dc current with the AWG and measure the dc voltage across the SNTJ with the oscilloscope (OSC), mounted in a 4-point probe configuration (and set with the $1 \, \text{M}\Omega$ input impedance).

2. Possible improvements

Ultimately, the bias tee (BT) and directional coupler (DC) presently placed at 30 mK and used to inject respectively the dc bias and rf pump, should be made more compatible with the scarce real estate of the millikelvin stage. That means, ideally, placing them 4 K. With off-the-shelf components, that would bring an additional 0.5 to 1 dB of insertion loss in front of the KI-TWPA, which would degrade the noise performance by a few Kelvins: the chain-added noise would then be around 10 K. This noise may still be suitable for qubit readout, where a quantum-limited pre-amplifier is often placed at the millikelvin stage, typically a Josephson device, which routinely achieves 20 to 25 dB of gain [13, 43]. This pre-amplifier would bring the 10 K chain-added noise below that of vacuum at the chains input. In the future, the BT and DC could be implemented on chip, together with the KI-TWPA, thereby reducing their insertion loss. Ultimately, this seems like a natural path forward. Note that any other traveling-wave parametric amplifier faces the same issue of pump delivery.

Note also that the 3.5-6.5 GHz range over which the KI-TWPA has gain depends on the periodic loading inside the KI-TWPAs transmission line, which determines the position of the pump frequency at which exponential gain is achieved [8]. This range can be adjusted by changing the periodic loading's design (its period and impedance). As such, there is no fundamental obstacle to
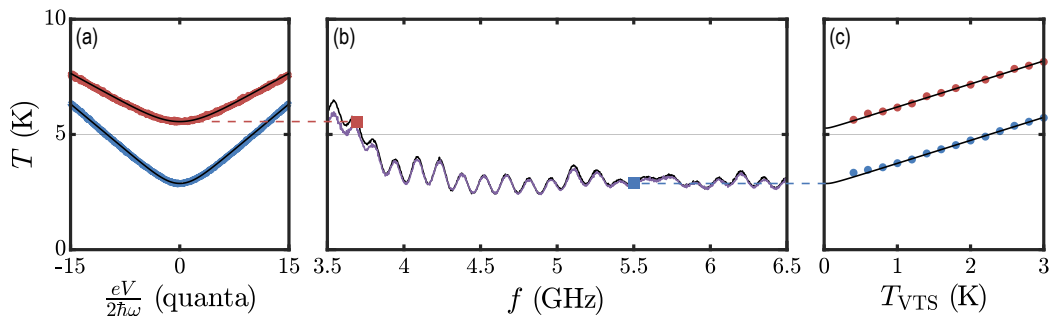
FIG. 7. Characterization of a HEMT-only amplifier chain (mounted at 4 K). (a) The output noise temperature is referred to the chain's input (i.e. divided by the chain's gain), and varies as a function of the SNTJ dc-bias voltage V. We illustrate the output noise recorded on the SA, in a 5 MHz window around two frequencies: 3.6 GHz (red curve) and 5.5 GHz (blue curve). We then retrieved the chain-added noise temperature $T_{\Sigma 2}$ from a fit (black curves). (b) Two techniques allow us to measure $T_{\Sigma 2}$ as a function of frequency: one using the shot noise generated by the dc-biased SNTJ (black curve), and one using the temperature-dependent Johnson noise generated by the unbiased SNTJ, mounted on a VTS (purple curve). Two squares underline the values of $T_{\Sigma 2}$: at 3.6 GHz, obtained with the shot noise method (red) and at 5.5 GHz, obtained with the Johnson noise method (blue). (c) The input-referred output noise temperature varies as a function of the VTS temperature. We illustrate this variation for two frequencies, 3.6 GHz (red points) and 5.5 GHz (blue points). We then recover $T_{\Sigma 2}$ from a fit (black lines).

have the same technology operate in the 6-10 GHz range, that is more favorable for qubit readout. Although dielectric loss will increase with frequency, so will the gain, for a fixed KI-TWPA length. Therefore, we don't expect the noise performance to be drastically different in the 6-10 GHz range, compared to what is shown in the present work.

Appendix D: 4 K HEMT amplification chain

We present in Fig. 8 an amplification chain, where the 4 K HEMT is the first amplifier. Compared to that of Fig. 6, several components have been removed from the signal path, notably the bias tees used to deliver the dc current I_d to the KI-TWPA, and the low-pass filter that protects the HEMT from the strong KI-TWPA rf pump tone. We chose to keep the isolator, because it is often placed before the HEMT in qubit experiments to avoid back-action [44] and in satellite mission concepts [19, 21], but we placed it at millikelvin temperatures to minimize its noise contribution. The unavoidable SNTJ packaging and bias tee remain in the chain.
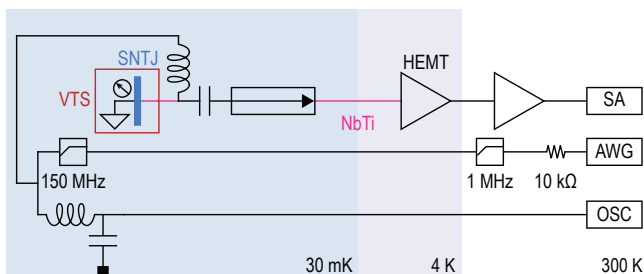

FIG. 8. Amplification chain where the HEMT is the first amplifier, placed at 4 K. The SNTJ (and its packaging) is mounted on a VTS.

Generating shot noise with the dc-biased SNTJ and fitting the output noise recorded on the SA [see Fig. 7(a)], we obtain $T_{\Sigma 2}$ as a function of frequency, shown in Fig. 7(b). To validate this result, we employed another, independent technique: in fact, at the chain's input the SNTJ (with its packaging) is mounted on a variable temperature stage (VTS), allowing us to generate a temperature-dependent Johnson noise with the unbiased SNTJ. Fitting the output noise [see Fig. 7(c)] we obtain a second estimate of $T_{\Sigma 2}$. Here, the chain's reference plane advances to the SNTJ packaging output, because the packaging's temperature also varies. Then, comparing the chain's gains between the two measurements (SNTJ and VTS), we estimate the SNTJ packaging insertion loss to be 0.3 ± 0.3 dB in the band of interest (see appendix F), similar to previous evaluations [45]. The quantitative agreement between both methods validate our use of the SNTJ as a calibrated noise source.

Appendix E: Fit of noise curves

1. Shot noise curves

We follow the same fitting procedure as in Ref. [8], but in the simpler case where we don't include the idler noise contribution. In short, the SNTJ delivers noise to the chain [8, 43], whose power is

$$
\begin{aligned}
N_{\text{in}}^s = \frac{k_B T}{2\hbar\omega_s} &\left[\frac{eV + \hbar\omega_s}{2k_B T} \coth\left(\frac{eV + \hbar\omega_s}{2k_B T} \right) \right. \\
&\left. + \frac{eV - \hbar\omega_s}{2k_B T} \coth\left(\frac{eV - \hbar\omega_s}{2k_B T} \right) \right],
\end{aligned}
\tag{E1}
$$

where T is the SNTJ temperature, V is the voltage across the SNTJ, and ω_s the signal frequency. The output noise

recorded on the SA is proportional to that of Eq. A9.

In practice, we first fit the output noise at high voltage V, for $|eV/(2\hbar\omega_s)| > 3$ quanta. In that case, Eq. E1 reduces to

$$N_{\text{in}}^s = \frac{eV}{2\hbar\omega_s}. \qquad (E2)$$

We obtain the chain's gain G_c and first estimation of N'_Σ.

Then we fit the central region, with G_c fixed. We let N'_Σ vary within $\pm 25\%$ of its first estimation, and because the AWG has a slight voltage offset V_{off}, we include it as a fit parameter: we write $V - V_{\text{off}}$ instead of V in Eq. E1. Finally, we bound T to a maximum value of 1 K.

2. Johnson noise curves

When varying the VTS temperature, we deliver noise to the chain whose power is

$$N_{\text{in}}^s = \frac{1}{2}\coth\left(\frac{\hbar\omega}{2k_B T_{\text{VTS}}}\right). \qquad (E3)$$

Knowing T_{VTS}, we fit the output noise recorded on the SA to get $N_{\Sigma 2} = T_{\Sigma 2}k_B/(\hbar\omega)$, the added noise of the chain containing only the HEMT at 4 K, see in appendix D.

Appendix F: Loss budget

We measured at 4 K the transmission of each part of the amplification chain with a VNA, to retrieve η_{1c}, η_{1h} and η_2 as a function of frequency see Fig. 9(a). To find η_{1c}, we first measured the transmission $\eta_{\alpha c}$ of the chain from the output of the SNTJ packaging to the input of the NbTi cable that connects the 30 mK stage to the 4 K stage. The SNTJ being a one-port device, we cannot measure directly the transmission of the SNTJ packaging η_{SNTJ}. Instead, we find it from the noise measurements performed on the chain solely containing the HEMT at 4 K: $\eta_{\text{SNTJ}} = 0.93 \pm 0.07$ is the ratio between the chain's gain obtained when using the SNTJ (proportional to $G_H\eta_2\eta_{1h}\eta_{\alpha c}\eta_{\text{SNTJ}}$) to the gain obtained when using the VTS (proportional to $G_H\eta_2\eta_{1h}\eta_{\alpha c}$). We then have $\eta_{1c} = \eta_{\alpha c}\eta_{\text{SNTJ}}$. The KI-TWPA packaging transmission η_p is measured separately at 4 K with a low probe tone power. It is then equally divided between η_{1h} and η_2. We report in Tab. IV the values of the various transmission efficiencies, along with their sub-components.

Knowing all the transmission efficiencies, we use Eq. A10 to deduce N_H, the HEMT-added noise at 70 K, from N'_Σ, the noise added by the chain presented in Fig. 1(b) (and measured with the SNTJ). In Fig. 9(b) we present $T_H = N_H\hbar\omega/k_B$ as a function of frequency, along with the manufacturer specifications for the HEMT-added noise, when the HEMT is at 4 K and 296 K [29]. Unsurprisingly, T_H lies between these two reported performances, with $T_H = 10.7 \pm 0.4$ K between 3.5 and

transmission efficiency	sub-component
$\eta_{1c} = 0.8 \pm 0.1$	$\eta_{\text{SNTJ}} = 0.93 \pm 0.07$
	$\eta_{\alpha c} = 0.86 \pm 0.05$
$\eta_{1h} = 0.8 \pm 0.1$	$\eta_{\alpha h} = 0.94 \pm 0.05$
	$\sqrt{\eta_p} = 0.85 \pm 0.1$
$\eta_2 = 0.51 \pm 0.1$	$\sqrt{\eta_p} = 0.85 \pm 0.1$
	$\eta_{\beta h} = 0.6 \pm 0.05$

TABLE IV. Transmission efficiencies at the various stages of the amplification chain and their sub-components, averaged between 3.5 and 5.5 GHz. In addition to the ones defined in the text, $\eta_{\alpha h}$ is the cable's transmission at 4 K, before the KI-TWPA, and $\eta_{\beta h}$ is the transmission of all the components between the KI-TWPA and the HEMT (see Fig. 6).
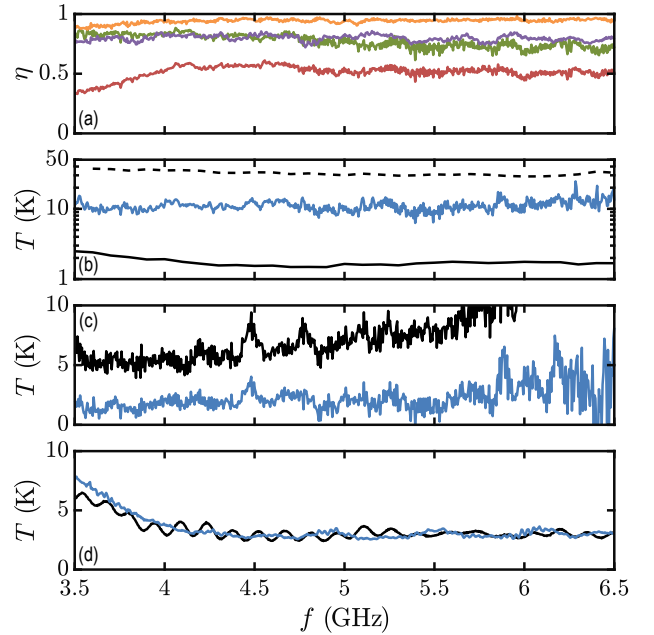

FIG. 9. Loss budget and inferred noise temperatures. (a) The transmission efficiencies η_{1c} (purple line), η_{1h} (green), η_2 (red) have been measured at 4 K. The SNTJ packaging transmission η_{SNTJ} (orange line) has been deduced from the ratio of chain's gains, obtained when using the SNTJ and the VTS. (b) The HEMT-added noise temperature T_H (blue line) is then deduced using Eq. A10. In comparison, we also show the noise temperature of the HEMT when it is at 4 K (solid black line) and 296 K (dashed black line). (c) The KI-TWPA-excess noise temperature T_{ex} (blue line) is then calculated with Eq. A8 using the data presented in (a) and (b), and using T_Σ (black line). (d) Both the measured (black line) and inferred (blue line) chain-added noise temperature $T_{\Sigma 2}$ agree quantitatively well. The inference is made from the manufacturer specification of the HEMT-added noise at 4 K and from transmission efficiency measurements on the parts of the chain shown in Fig. 8.

5.5 GHz (uncertainty dominated by that of the transmission efficiencies).

Then, using Eq. A8 we deduce N_{ex}, the KI-TWPA-excess noise. In Fig. 9(c) we show $T_{ex} = N_{ex}\hbar\omega/k_B$, along with T_Σ, as a function of frequency. In the 3.5-5.5 GHz band we have $T_{ex} = 1.9 \pm 0.2$ K.
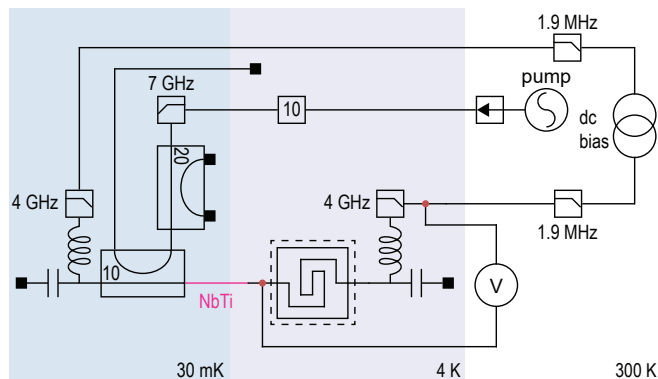

FIG. 10. Four-point probe experimental setup. Two red points highlight the ports across which we measure the voltage drop while the KI-TWPA is under dc and rf biases.

Finally, we also measured (at 4 K) the transmission efficiencies of each parts of the chain presented in Fig. 8, where the HEMT is mounted at 4 K. Then, from the manufacturer specification of the HEMT-added noise at 4 K [see Fig. 9(b)] we calculated the expected chain-added noise, and compared it to the measured one, see Fig. 9(d). Both are in good quantitative agreement, validating our overall methodology for the loss budget.

Appendix G: Four-point probe setup

We present in Fig. 10 the experimental setup used to evaluate the dc power consumption of the KI-TWPA. With the KI-TWPA under dc and rf biases, we measure the voltage drop between components at 4 K required to operate the KI-TWPA, consisting of the KI-TWPA itself, the BT, and the LPF placed after the dc input of the BT. At room temperature, a voltmeter reads the voltage across these components. Note that we have terminated the rf amplification chain at 4 K, because it is not properly matched to $50\,\Omega$ anymore: in fact, we inserted a subminiature version A (SMA) T-junction at the KI-TWPA input in order to read the potential at this point.

[1] B. Yurke, L. R. Corruccini, P. G. Kaminsky, L. W. Rupp, A. D. Smith, A. H. Silver, R. W. Simon, and E. A. Whittaker, "Observation of parametric amplification and deamplification in a Josephson parametric amplifier," Phys. Rev. A **39**, 2519–2533 (1989).

[2] M. A. Castellanos-Beltran, K. D. Irwin, G. C. Hilton, L. R. Vale, and K. W. Lehnert, "Amplification and squeezing of quantum noise with a tunable Josephson metamaterial," Nature Physics **4**, 929–931 (2008).

[3] N. Bergeal, F. Schackert, M. Metcalfe, R. Vijay, V. E. Manucharyan, L. Frunzio, D. E. Prober, R. J. Schoelkopf, S. M. Girvin, and M. H. Devoret, "Phase-preserving amplification near the quantum limit with a Josephson ring modulator," Nature **465**, 64–68 (2010).

[4] B. H. Eom, P. K. Day, H. G. LeDuc, and J. Zmuidzinas, "A wideband, low-noise superconducting amplifier with high dynamic range," Nature Physics **8**, 623–627 (2012).

[5] C. Macklin, K. O'Brien, D. Hover, M. E. Schwartz, V. Bolkhovsky, X. Zhang, W. D. Oliver, and I. Siddiqi, "A near–quantum-limited Josephson traveling-wave parametric amplifier," Science **350**, 307–310 (2015).

[6] N. E. Frattini, U. Vool, S. Shankar, A. Narla, K. M. Sliwa, and M. H. Devoret, "3-wave mixing Josephson dipole element," Applied Physics Letters **110**, 222603 (2017).

[7] L. Planat, A. Ranadive, R. Dassonneville, J. Puertas Martínez, S. Léger, C. Naud, O. Buisson, W. Hasch-Guichard, D.M. Basko, and N. Roch, "Photonic-crystal Josephson traveling-wave parametric amplifier," Phys. Rev. X **10**, 021021 (2020).

[8] M. Malnou, M.R. Vissers, J.D. Wheeler, J. Aumentado, J. Hubmayr, J.N. Ullom, and J. Gao, "Three-wave mixing kinetic inductance traveling-wave amplifier with near-quantum-limited noise performance," PRX Quantum **2**, 010302 (2021).

[9] M. Malnou, D. A. Palken, Leila R. Vale, Gene C. Hilton, and K. W. Lehnert, "Optimal operation of a Josephson parametric amplifier for vacuum squeezing," Phys. Rev. Applied **9**, 044023 (2018).

[10] S. Chaudhuri, D. Li, K. D. Irwin, C. Bockstiegel, J. Hubmayr, J. N. Ullom, M. R. Vissers, and J. Gao, "Broadband parametric amplifiers based on nonlinear kinetic inductance artificial transmission lines," Applied Physics Letters **110**, 152601 (2017).

[11] S. Shu, N. Klimovich, B. H. Eom, A. D. Beyer, R. Basu Thakur, H. G. Leduc, and P. K. Day, "Nonlinearity and wide-band parametric amplification in a (Nb,Ti)N microstrip transmission line," Phys. Rev. Research **3**, 023184 (2021).

[12] Daniel J Parker, Mykhailo Savytskyi, Wyatt Vine, Arne Laucht, Timothy Duty, Andrea Morello, Arne L Grimsmo, and Jarryd J Pla, "A near-ideal degenerate parametric amplifier," arXiv preprint arXiv:2108.10471 (2021).

[13] Frank Arute, Kunal Arya, Ryan Babbush, Dave Bacon, Joseph C. Bardin, Rami Barends, Rupak Biswas, Sergio Boixo, Fernando G. S. L. Brandao, David A. Buell, Brian Burkett, Yu Chen, Zijun Chen, Ben Chiaro, Roberto Collins, William Courtney, Andrew Dunsworth, Edward Farhi, Brooks Foxen, Austin Fowler, Craig Gidney, Marissa Giustina, Rob Graff, Keith Guerin, Steve Habegger, Matthew P. Harrigan, Michael J. Hartmann, Alan Ho, Markus Hoffmann, Trent Huang, Travis S. Humble, Sergei V. Isakov, Evan Jeffrey, Zhang Jiang, Dvir Kafri, Kostyantyn Kechedzhi, Julian Kelly, Paul V. Klimov, Sergey Knysh, Alexander Korotkov, Fedor Kostritsa,

David Landhuis, Mike Lindmark, Erik Lucero, Dmitry Lyakh, Salvatore Mandrà, Jarrod R. McClean, Matthew McEwen, Anthony Megrant, Xiao Mi, Kristel Michielsen, Masoud Mohseni, Josh Mutus, Ofer Naaman, Matthew Neeley, Charles Neill, Murphy Yuezhen Niu, Eric Ostby, Andre Petukhov, John C. Platt, Chris Quintana, Eleanor G. Rieffel, Pedram Roushan, Nicholas C. Rubin, Daniel Sank, Kevin J. Satzinger, Vadim Smelyanskiy, Kevin J. Sung, Matthew D. Trevithick, Amit Vainsencher, Benjamin Villalonga, Theodore White, Z. Jamie Yao, Ping Yeh, Adam Zalcman, Hartmut Neven, and John M. Martinis, "Quantum supremacy using a programmable superconducting processor," Nature **574**, 505–510 (2019).

[14] B. M. Brubaker, L. Zhong, Y. V. Gurevich, S. B. Cahn, S. K. Lamoreaux, M. Simanovskaia, J. R. Root, S. M. Lewis, S. Al Kenany, K. M. Backes, I. Urdinaran, N. M. Rapidis, T. M. Shokair, K. A. van Bibber, D. A. Palken, M. Malnou, W. F. Kindel, M. A. Anil, K. W. Lehnert, and G. Carosi, "First results from a microwave cavity axion search at 24 μeV," Phys. Rev. Lett. **118**, 061302 (2017).

[15] N. Du, N. Force, R. Khatiwada, E. Lentz, R. Ottens, L. J Rosenberg, G. Rybka, G. Carosi, N. Woollett, D. Bowring, A. S. Chou, A. Sonnenschein, W. Wester, C. Boutan, N. S. Oblath, R. Bradley, E. J. Daw, A. V. Dixit, J. Clarke, S. R. O'Kelley, N. Crisosto, J. R. Gleason, S. Jois, P. Sikivie, I. Stern, N. S. Sullivan, D. B Tanner, and G. C. Hilton (ADMX Collaboration), "Search for invisible axion dark matter with the axion dark matter experiment," Phys. Rev. Lett. **120**, 151301 (2018).

[16] K. M. Backes, D. A. Palken, S. Al Kenany, B. M. Brubaker, S. B. Cahn, A. Droster, Gene C. Hilton, Sumita Ghosh, H. Jackson, S. K. Lamoreaux, A. F. Leder, K. W. Lehnert, S. M. Lewis, M. Malnou, R. H. Maruyama, N. M. Rapidis, M. Simanovskaia, Sukhman Singh, D. H. Speller, I. Urdinaran, Leila R. Vale, E. C. van Assendelft, K. van Bibber, and H. Wang, "A quantum enhanced search for dark matter axions," Nature **590**, 238–242 (2021).

[17] B. Dober, D. T. Becker, D. A. Bennett, S. A. Bryan, S. M. Duff, J. D. Gard, J. P. Hays-Wehle, G. C. Hilton, J. Hubmayr, J. A. B. Mates, C. D. Reintsema, L. R. Vale, and J. N. Ullom, "Microwave squid multiplexer demonstration for cosmic microwave background imagers," Applied Physics Letters **111**, 243510 (2017).

[18] C. R. H. McRae, H. Wang, J. Gao, M. R. Vissers, T. Brecht, A. Dunsworth, D. P. Pappas, and J. Mutus, "Materials loss measurements using superconducting microwave resonators," Review of Scientific Instruments **91**, 091101 (2020).

[19] Simon R. Bandler, James A. Chervenak, Aaron M. Datesman, Archana M. Devasia, Michael J. DiPirro, Kazuhiro Sakai, Stephen J. Smith, Thomas R. Stevenson, Wonsik Yoon, Douglas A. Bennett, Benjamin Mates, Daniel S. Swetz, Joel N. Ullom, Kent D. Irwin, Megan E. Eckart, Enectali Figueroa-Feliciano, Dan McCammon, Kevin K. Ryu, Jeffrey R. Olson, and Ben Zeiger, "Lynx x-ray microcalorimeter," Journal of Astronomical Telescopes, Instruments, and Systems **5**, 1 – 29 (2019).

[20] Michael DiPirro, Simon Bandler, Xiaoyi Li, Jeffrey Olson, James Tuttle, Wonsik Yoon, and Mark Zagarola, "Lynx x-ray microcalorimeter cryogenic system," Journal of Astronomical Telescopes, Instruments, and Systems **5**, 1 – 8 (2019).

[21] Pierre M. Echternach, Andrew D. Beyer, and Charles M. Bradford, "Large array of low-frequency readout quantum capacitance detectors," Journal of Astronomical Telescopes, Instruments, and Systems **7**, 1 – 8 (2021).

[22] Damon C. Bradley, Tracee L. Jamison-Hooks, Johannes G. Staguhn, Edward G. Amatucci, Tyler Browning, Michael J. DiPirro, David T. Leisawitz, and Ruth C. Carter, "On the advancements of digital signal processing hardware and algorithms enabling the Origins Space Telescope," Journal of Astronomical Telescopes, Instruments, and Systems **7**, 1 – 13 (2021).

[23] Martina C. Wiedner, Susanne Aalto, Edward G. Amatucci, Andrey M. Baryshev, Cara Battersby, Victor Y. Belitsky, Edwin Bergin, Bruno Borgo, Ruth C. Carter, Emmanuel Caux, Asantha Cooray, James A. Corsetti, Elvire De Beck, Yan Delorme, Vincent Pierre Desmaris, Michael J. DiPirro, Brian N. Ellison, Anna Maria Di Giorgio, Martin J. Eggens, Juan Daniel Gallego-Puyol, Maryvonne Gerin, Paul F. Goldsmith, Christophe Goldstein, Frank P. Helmich, Fabrice Herpin, Richard E. Hills, Michiel Hogerheijde, Leslie K. Hunt, Willem Jellema, Geert Keizer, Jean-Michel Krieg, Gabby Kroes, Philippe Laporte, Andr Laurens, David T. Leisawitz, Dariusz C. Lis, Gregory E. Martins, Imran Mehdi, Margaret Meixner, Gary J. Melnick, Stefanie N. Milam, David A. Neufeld, Napolon Nguyen-Tuong, Rn Plume, Klaus Pontoppidan, Benjamin Quertier-Dagorn, Christophe Risacher, Johannes G. Staguhn, Edward Tong, Serena Viti, Friedrich Wyrowski, and The Origins Space Telescope Mission Concept Study Team, "Heterodyne Receiver for Origins," Journal of Astronomical Telescopes, Instruments, and Systems **7**, 1 – 24 (2021).

[24] NASA, "2020 decadal survey planning," (2021).

[25] N. Zobrist, B. H. Eom, P. Day, B. A. Mazin, S. R. Meeker, B. Bumble, H. G. LeDuc, G. Coiffard, P. Szypryt, N. Fruitwala, I. Lipartito, and C. Bockstiegel, "Wideband parametric amplifier readout and resolution of optical microwave kinetic inductance detectors," Applied Physics Letters **115**, 042601 (2019).

[26] M. R. Vissers, R. P. Erickson, H.-S. Ku, L. Vale, X. Wu, G. C. Hilton, and D. P. Pappas, "Low-noise kinetic inductance traveling-wave amplifier using three-wave mixing," Applied Physics Letters **108**, 012601 (2016).

[27] Jonas Zmuidzinas, "Superconducting microresonators: Physics and applications," Annual Review of Condensed Matter Physics **3**, 169–214 (2012).

[28] L. Ranzani, M. Bal, Kin Chung Fong, G. Ribeill, X. Wu, J. Long, H.-S. Ku, R. P. Erickson, D. Pappas, and T. A. Ohki, "Kinetic inductance traveling-wave amplifiers for multiplexed qubit readout," Applied Physics Letters **113**, 242602 (2018).

[29] https://www.lownoisefactory.com/datasheets/LNF-LNC4_8C_sn1315H.pdf.

[30] Carlton M. Caves, "Quantum limits on noise in linear amplifiers," Phys. Rev. D **26**, 1817–1839 (1982).

[31] Jeffrey M. Epstein, K. Birgitta Whaley, and Joshua Combes, "Quantum limits on noise for a class of nonlinear amplifiers," Phys. Rev. A **103**, 052415 (2021).

[32] Y. Yamamoto and K. Inoue, "Noise in amplifiers," Journal of Lightwave Technology **21**, 2895–2915 (2003).

[33] L. Spietz, R. J. Schoelkopf, and P. Pari, "Shot noise thermometry down to 10mk," Applied Physics Letters **89**, 183123 (2006).

[34] P. Szypryt, S. R. Meeker, G. Coiffard, N. Fruitwala, B. Bumble, G. Ulbricht, A. B. Walter, M. Daal, C. Bockstiegel, G. Collura, N. Zobrist, I. Lipartito, and B. A. Mazin, "Large-format platinum silicide microwave kinetic inductance detectors for optical to near-ir astronomy," Opt. Express **25**, 25894–25909 (2017).

[35] K. D. Irwin and K. W. Lehnert, "Microwave squid multiplexer," Applied Physics Letters **85**, 2107–2109 (2004).

[36] J. A. B. Mates, D. T. Becker, D. A. Bennett, B. J. Dober, J. D. Gard, J. P. Hays-Wehle, J. W. Fowler, G. C. Hilton, C. D. Reintsema, D. R. Schmidt, D. S. Swetz, L. R. Vale, and J. N. Ullom, "Simultaneous readout of 128 x-ray and gamma-ray transition-edge microcalorimeters using microwave squid multiplexing," Applied Physics Letters **111**, 062601 (2017).

[37] L. Spietz, K. W. Lehnert, I. Siddiqi, and R. J. Schoelkopf, "Primary electronic thermometry using the shot noise of a tunnel junction," Science **300**, 1929–1932 (2003).

[38] Eunjung Cha, Niklas Wadefalk, Giuseppe Moschetti, Arsalan Pourkabirian, Jrgen Stenarson, and Jan Grahn, "A 300-w cryogenic hemt lna for quantum computing," in *2020 IEEE/MTT-S International Microwave Symposium (IMS)* (2020) pp. 1299–1302.

[39] J. Bockstiegel, C.and Gao, M.R. Vissers, M. Sandberg, S. Chaudhuri, A. Sanders, L.R. Vale, K.D. Irwin, and D.P. Pappas, "Development of a broadband NbTiN traveling wave parametric amplifier for mkid readout," Journal of Low Temperature Physics **176**, 476–482 (2014).

[40] Arpit Ranadive, Martina Esposito, Luca Planat, Edgar Bonet, Cécile Naud, Olivier Buisson, Wiebke Guichard, and Nicolas Roch, "A reversed Kerr traveling wave parametric amplifier," arXiv preprint arXiv:2101.05815 (2021).

[41] M. Houde, L.C.G. Govia, and A.A. Clerk, "Loss asymmetries in quantum traveling-wave parametric amplifiers," Phys. Rev. Applied **12**, 034054 (2019).

[42] Robert W Boyd, *Nonlinear optics* (Academic press, 2019).

[43] F. Lecocq, L. Ranzani, G. A. Peterson, K. Cicak, R. W. Simmonds, J. D. Teufel, and J. Aumentado, "Nonreciprocal microwave signal processing with a field-programmable Josephson amplifier," Phys. Rev. Applied **7**, 024028 (2017).

[44] Eric I. Rosenthal, Christian M. F. Schneider, Maxime Malnou, Ziyi Zhao, Felix Leditzky, Benjamin J. Chapman, Waltraut Wustmann, Xizheng Ma, Daniel A. Palken, Maximilian F. Zanner, Leila R. Vale, Gene C. Hilton, Jiansong Gao, Graeme Smith, Gerhard Kirchmair, and K. W. Lehnert, "Efficient and low-backaction quantum measurement using a chip-scale detector," Phys. Rev. Lett. **126**, 090503 (2021).

[45] S.-W. Chang, J. Aumentado, W.-T. Wong, and J.C. Bardin, "Noise measurement of cryogenic low noise amplifiers using a tunnel-junction shot-noise source," in *2016 IEEE MTT-S International Microwave Symposium (IMS)* (IEEE, 2016) pp. 1–4.